



COOL-LAMPS. II. Characterizing the Size and Star Formation History of a Bright Strongly Lensed Early-type Galaxy at Redshift 1.02

Ezra Sukay^{1,2}, Gourav Khullar^{1,3}, Michael D. Gladders^{1,3}, Keren Sharon⁴, Guillaume Mahler^{4,5}, Kate Napier⁴, Lindsey E. Bleem^{3,6}, Håkon Dahle⁷, Michael K. Florian⁸, Katya Gozman^{1,4}, Jason J. Lin¹, Michael N. Martinez¹, Owen S. Matthews Acuña¹, Elisabeth Medina¹, Kaiya Merz¹, Jorge A. Sanchez¹, Emily E. Sisco¹, Daniel J. Kavlin Stein¹, Kiyan Tavangar¹, and Katherine E. Whitaker^{9,10}

¹ Department of Astronomy and Astrophysics, University of Chicago, 5640 South Ellis Avenue, Chicago, IL 60637, USA; esukay1@jhu.edu

² Department of Physics and Astronomy, Johns Hopkins University, 3400 North Charles Street, Baltimore, MD 21218, USA

³ Kavli Institute for Cosmological Physics, University of Chicago, 5640 South Ellis Avenue, Chicago, IL 60637, USA

⁴ Department of Astronomy, University of Michigan, 1085 South University Drive, Ann Arbor, MI 48109, USA

⁵ Department of Physics, Durham University, South Road, Durham DH1 3LE, UK

⁶ Argonne National Laboratory, High-Energy Physics Division, 9700 South Cass Avenue, Argonne, IL 60439, USA

⁷ Institute of Theoretical Astrophysics, University of Oslo, P.O. Box 1029, Blindern, NO-0315 Oslo, Norway

⁸ Steward Observatory, University of Arizona, 933 North Cherry Avenue, Tucson, AZ 85721, USA

⁹ Department of Astronomy, University of Massachusetts, Amherst, MA 01003, USA

¹⁰ Cosmic Dawn Center (DAWN), Copenhagen, Denmark

Received 2022 March 22; revised 2022 September 28; accepted 2022 October 3; published 2022 November 18

Abstract

We present COOL J1323+0343, an early-type galaxy at $z = 1.0153 \pm 0.0006$, strongly lensed by a cluster of galaxies at $z = 0.353 \pm 0.001$. This object was originally imaged by DECaLS and noted as a gravitational lens by COOL-LAMPS, a collaboration initiated to find strong-lensing systems in recent public optical imaging data, and confirmed with follow-up data. With ground-based *grzH* imaging and optical spectroscopy from the Las Campanas Observatory and the Nordic Optical Telescope, we derive a stellar mass, metallicity, and star formation history from stellar-population synthesis modeling. The lens modeling implies a total magnification, summed over the three images in the arc, of $\mu \sim 113$. The stellar mass in the source plane is $M_* \sim 10.64 M_\odot$ and the 1σ upper limit on the star formation rate (SFR) in the source plane is $\text{SFR} \sim 3.75 \times 10^{-2} M_\odot \text{ yr}^{-1}$ ($\log \text{sSFR} = -12.1 \text{ yr}^{-1}$) in the youngest two age bins (0–100 Myr), closest to the epoch of observation. Our measurements place COOL J1323+0343 below the characteristic mass of the stellar mass function, making it an especially compelling target that could help clarify how intermediate-mass quiescent galaxies evolve. We reconstruct COOL J1323+0343 in the source plane and fit its light profile. This object is below the expected size evolution of an early-type galaxy at this mass with an effective radius $r_e \sim 0.5 \text{ kpc}$. This extraordinarily magnified and bright lensed early-type galaxy offers an exciting opportunity to study the morphology and star formation history of an intermediate-mass early-type galaxy in detail at $z \sim 1$.

Unified Astronomy Thesaurus concepts: Early-type galaxies (429); Elliptical galaxies (456); Galaxy evolution (594); High-redshift galaxies (734); Quenched galaxies (2016); Galaxy quenching (2040); Spectral energy distribution (2129); Strong gravitational lensing (1643); Galaxy spectroscopy (2171)

1. Introduction

Untangling the mechanisms that fuel the evolution of early-type galaxies (ETGs) is a key component to understanding how the diverse population of galaxies in the local universe formed. The discovery that ETGs at $z > 1$ are much more compact than those in the local universe, with radii between three and five times smaller without much change in mass, is a challenge to our understanding of galaxy evolution (Daddi et al. 2005; Trujillo et al. 2006, 2007; van Dokkum et al. 2008; Newman et al. 2010). There are two theories proposed to explain this growth: First, mergers with small, gas-poor satellite galaxies known as minor mergers. Second, internal mechanisms like adiabatic expansion. Minor dry mergers would increase the radii of ETGs without requiring the addition of a proportional amount of mass (Bezanson et al. 2009; Naab et al. 2009) and some studies found that they are consistent with observations

of ETGs at $z < 1.6$ (Belli et al. 2014). Minor mergers may explain the evolution seen at low redshifts, but they are insufficient to explain the rapid evolution and the scatter in radii at higher redshifts (Fan et al. 2010; Newman et al. 2012; Nipoti et al. 2012). Furthermore, surveys have struggled to find the number of companion satellites required (Newman et al. 2012). Adiabatic expansion triggered by active galactic nuclei feedback, in combination with dry mergers, might resolve these inconsistencies (Fan et al. 2010). Recent work by Suess et al. (2019a, 2019b) analyzing color gradients indicates that the half mass–radius of galaxies does not grow at the same rate as the half light radius, which would also make minor merger scenarios more feasible.

Another potential explanation is progenitor bias; the idea that the processes that quench ETGs at lower redshifts are different from those at $z > 2$ and, as a result, latecomers to the ETG population have larger radii. Number density studies found strong evidence that progenitor bias is not sufficient to explain the growth of massive ETGs (Newman et al. 2010; Belli et al. 2014, 2015). For intermediate-mass ETGs (those with $10.5 < \log M_* < 11$), some studies found that progenitor bias explains



Original content from this work may be used under the terms of the [Creative Commons Attribution 4.0 licence](https://creativecommons.org/licenses/by/4.0/). Any further distribution of this work must maintain attribution to the author(s) and the title of the work, journal citation and DOI.

the majority of the observed evolution after $z = 1$ (Carollo et al. 2013; Fagioli et al. 2016). However, many other studies found evidence that individual growth is needed, at least in part, to explain the growth of intermediate-mass ETGs (Cassata et al. 2011; Newman et al. 2012; Whitaker et al. 2012; Belli et al. 2014; van der Wel et al. 2014; Belli et al. 2015).

The mechanisms that fuel the evolution of ETGs after they quench affects the morphology of evolving objects. Dry mergers with low-mass objects result in central regions that have similar densities to very compact ETGs at $z \sim 2$, with an envelope of low-density material, high Sérsic indices ($n \geq 5$), and negative metallicity gradients (Hopkins et al. 2009; Hilz et al. 2013). Adiabatic processes caused by quasar feedback would make the central regions of ETGs less dense in the local universe than they are at $z \sim 2$ (Fan et al. 2010). In-depth morphological studies will also provide clues to how ETGs quench in the first place. Simulations suggest galaxies that quenched “inside-out” through a central starburst have younger central stars than those on the edge (Wellons et al. 2015). However, galaxies that quenched “outside-in” through cold gas accretion have stellar ages that are the same throughout or older central stars (Feldmann et al. 2016).

Spatially resolved imaging and spectroscopy targeting ETGs from $0.5 < z < 2$ should allow us to understand how they quench and what processes drive their structural evolution after star formation ceases. It is difficult to spatially resolve the most compact systems that may be little-modified descendants of compact high-redshift ETGs (e.g., Stockton et al. 2014). Strong gravitational lensing enables the study of more representative quiescent galaxies with better spatial resolution and signal to noise (e.g., Oldham et al. 2017; Akhshik et al. 2020, 2021; Man et al. 2021). Taking advantage of lensing magnification, Akhshik et al. (2020, 2021) and Jafariyazani et al. (2020) took spatially resolved spectra of massive quiescent galaxies at $z \sim 2$, enabling them to measure age and metallicity gradients. More examples of lensed ETGs, particularly with large magnifications that enable detailed studies, are key to further progress.

We discuss here the discovery and initial characterization of COOL J1323+0343: a compact intermediate-mass ETG with old stellar populations that would be near impossible to study in-depth without strong gravitational lensing. COOL J1323+0343’s extraordinary magnification of $\mu > 100$ offers the opportunity to study a representative ETG at $z \sim 1$, and makes it an especially compelling target for more detailed follow-up imaging and spectroscopy.

This Paper is structured as follows. Section 2 briefly describes the discovery of COOL J1323+0343. Section 3 describes the follow-up imaging and spectroscopy of COOL J1323+0343. In Section 4, we report the results of stellar-population synthesis modeling. The lens modeling and source plane reconstruction are described in Section 5. Section 6 puts COOL J1323+0343 in context with other ETGs and discusses what we expect to learn from detailed follow-up.

All reported magnitudes are calibrated to the AB system. The fiducial cosmology model used assumes a standard flat cold dark-matter model with a cosmological constant (Λ CDM), corresponding to WMAP9 observations (Hinshaw et al. 2013). For inferred parameters with uncertainties, we report 16th, 50th, and 84th percentile values, unless otherwise specified.

2. Discovery

COOL J1323+0343 (hereafter CJ 1323; 13h23m04^s.12 03°43′19″.4) was discovered in a search for strong lenses in the Dark Energy Camera Legacy Survey (DECaLS) data release 8 (DR8; Dey et al. 2019) by Chicago Optically-selected strong Lenses—Located At the Margins of Public Surveys (COOL-LAMPS). Details about this search and results will be described in a future publication, so we only provide brief details here.

We found CJ 1323 as part of a comprehensive visual search of the northern galactic cap portion of the southern DECaLS data set. Specifically, CJ 1323 was found in a search that examined lines of sight centered on luminous red galaxies, out to a photometric redshift of $z \sim 0.7$. Both the foreground lensing cluster and the lensed source were immediately apparent in the DECaLS images; six coauthors examined this particular field yielding an aggregate score of 2.4 on a scale of zero to three, where a score of three signifies a definite lens.

The foreground lens was first noted as a cluster by Hao et al. (2010) and was included in several other more recent cluster catalogs (e.g., Rykoff et al. 2014; Hilton et al. 2021). CJ 1323 was independently discovered as a strong-lensing candidate by Huang et al. (2021), and noted as DESI-200.7678+03.7216. They first searched DR7 with a residual neural network (Lanusse et al. 2018) using a training sample consisting of only observed images, but did not find this lens (Huang et al. 2020). Using an improved “shielded” model with a larger training set on the complete DR8 data set, the neural net presented in Huang et al. (2021) gave CJ 1323 a probability of 0.34, well above their threshold of 0.1. Through visual inspection, it was assigned a final grade of four on a scale of one to four, which indicates it is among the systems showing the clearest evidence of strong lensing.

3. Follow-up Observations and Analysis

3.1. Imaging

Near-infrared imaging of CJ 1323 in the H band was obtained using the FourStar Infrared Camera (FOURSTAR; Persson et al. 2008) on the Magellan/Baade telescope, in Chile, on 2020 February 22. The total integration time was 183 s; the apparent brightness despite the brevity of this total time is a testament to the brightness of the lensed source images. We reduced the data to final astrometrically and photometrically calibrated stacked images using a custom pipeline built via IRAF (Tody 1986, 1993) and PHOTPIPE (Rest et al. 2005; Garg et al. 2007; Miknaitis et al. 2007). We show a color image combining the H -band image with the DECaLS grz data in Figure 1.

The H -band image was calibrated to Two Micron All Sky Survey (2MASS) stars (Skrutskie et al. 2006) within the field of view, with the calibration derived automatically by PHOTPIPE routines. Uncertainty on the zero-point relative to 2MASS is ~ 0.02 mag. We used the provided zero-points for the DECaLS data; the uncertainties on these values were insignificant compared to other measurement uncertainties.

While the photometric analysis in this Paper was completed primarily with the DECaLS optical imaging and FOURSTAR near-IR imaging, late in the preparation of this manuscript we obtained grz -band imaging. The images were taken with the low-dispersion survey spectrograph (LDSS3¹¹) on the Magellan/Baade telescope, in Chile, on 2021 January 16, for a total

¹¹ http://www.lco.cl/?epkb_post_type_1=ldss-3-user-manual

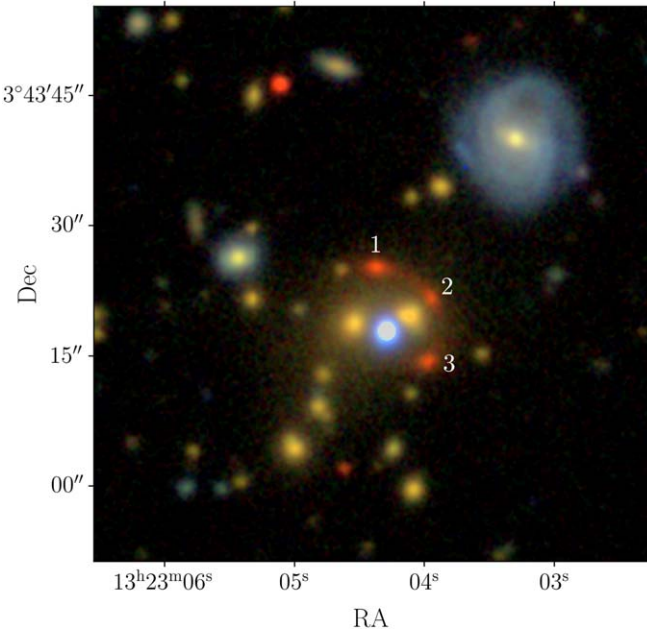


Figure 1. $gr(z + H)$ image of COOL J1323+0343. This image was constructed using grz -band imaging from DECaLS and H -band imaging from FOURSTAR on Magellan. The lensed galaxy is seen as a bright red multiply imaged source, with three images. We refer to the images by number throughout the Paper, corresponding to the labels in this figure. The foreground cluster has two similarly bright central galaxies. The bright blue source between the two brightest cluster galaxies is a foreground star.

integration time of 360 s per filter, in subarcsecond seeing conditions. These higher resolution images were used to confirm the lensing configuration implied by the earlier data, as described in Section 5.

3.2. Spectroscopy

Spectroscopic observations of CJ 1323 were obtained on 2020 April 19, using the Alhambra Faint Object Spectrograph and Camera (ALFOSC) at the 2.56 m Nordic Optical Telescope (NOT). Two 2400 s exposures were obtained using grism #20 ($R = 590$, $\lambda = 5650\text{--}10, 150\text{\AA}$), using a $1/3$ longslit. Halogen lamps were used for spectroscopic flat fielding, and wavelength solutions were calibrated using HeNe and ThAr arc lamps. Spectrophotometric calibration was performed using observations of the standard star SP 1045+378. The longslit was placed to sample the most northern and most southern apparent images of the lensed source, and a dither along the slit was made between the two exposures sufficient to place both spectra of the source on slit regions that were clear of other objects.

Reduction to one-dimensional wavelength- and flux-calibrated spectra was accomplished using standard routines in IRAF. Sky subtraction was ultimately accomplished using A-B subtraction of the two dithered spectra; while we explored sky subtraction using adjacent sky apertures, we found they gave poor results. Light from the star and lens galaxy in between the two source images (see Figure 1) contaminates regions that might otherwise be used as sky apertures and limits the accuracy with which the sky can be subtracted in this case.

3.3. Redshifts

CJ 1323 is lensed by GMBG J2007+03722 (Hao et al. 2010), a galaxy cluster indicated by the abundance of

red-sequence galaxies (Gladders & Yee 2000) easily visible in Figure 1 as elliptical galaxies with a similar orange hue. The two brightest of these galaxies near the cluster center have redshifts reported in the Sloan Digital Sky Survey (SDSS) Legacy Survey at $z = 0.3535 \pm 0.0001$ (York et al. 2000; Strauss et al. 2002) and by BOSS at $z = 0.35256 \pm 0.00006$ (Eisenstein et al. 2011; Dawson et al. 2013) for the east and west galaxies, respectively. We took the cluster redshift as the average of these two values.

The redshift of the lensed galaxy CJ 1323 is $z = 1.0153 \pm 0.0006$, based on Ca H & K, H- δ , and G -band features clearly visible in the NOT-ALFOSC spectrum shown in the bottom panel of Figure 2.

3.4. Model Photometry with GALFIT

We used the parametric fitting code GALFIT (Peng et al. 2002, 2010) to fit light profiles to lensing cluster galaxies, other line-of-sight contaminants, and the targets of interest. For the H band, we followed the process for making point-spread functions (PSFs) and utilizing GALFIT as described in Khullar et al. (2021). We used one or more two-dimensional Sérsic components to model the light of the components of the arc, galaxy cluster, and other objects. The foreground star between the cluster galaxies was fitted with a PSF and an additional Sérsic component to account for residual differences between this star and nearby isolated stars that were used to construct a reference PSF. Statistical magnitude uncertainties were measured as described in Khullar et al. (2021), with the final best-fit model image injected into blank regions of the image, and then refit, with the distributions of results from these inject-and-recover tests providing the uncertainties. Additionally, models were built independently by three coauthors, and we found that the systematic uncertainties induced by the decision process inherent in this type of iterative model building were insignificant for the H -band measurements.

However, a similar initial analysis of the coarser DECaLS imaging—in particular, the comparison of results from the three independent models—indicated a significant issue with modeling systematics. The precise origin of this problem is unclear, but we suspect it is related to the crowded complexity of the central lens regions and the much poorer seeing in the DECaLS data relative to the H -band. In particular, due to the overlapping mosaic of sampling from individual integrations that comprise the DECaLS images, there was no nearby isolated bright star to use as a reference, and hence in these data we were forced to use the star in the center of the field as a PSF reference. This was accomplished by first fitting the central region with a GALFIT model, absent of any PSF convolution, with the star itself described by a two-component Moffat profile. The best-fit model of the star was then extracted and used as a PSF reference for a complete GALFIT model of field. This limitation was possibly the source of the observed systematic differences between completed models.

As an alternate measurement, we used GALFIT to fit nearby galaxies and stars with the targeted lensed images masked so that, after modeling, only the arc remained in the residual image. The photometry was then measured from this residual image using complex arc-like apertures at various scales, in order to measure the photometric curve of growth and a total lensed image magnitude (e.g., Wuyts et al. 2010). This second approach produced internally consistent results. In the

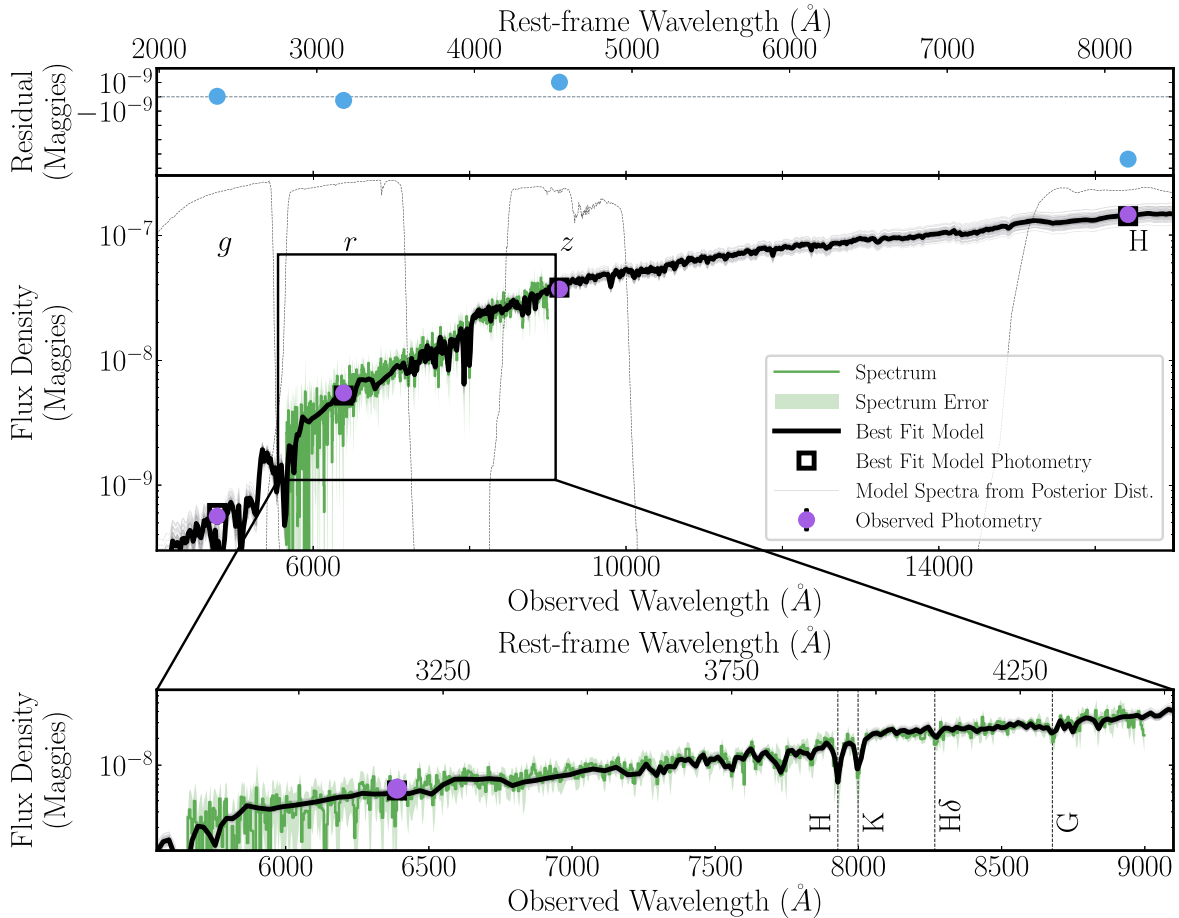


Figure 2. (Top) Residual between the best-fit Prospector model and the observed photometry (blue). (Middle) Best-fit SED model using the Kriek & Conroy (2013) dust attenuation curve (black) and other fits from the posterior distribution (gray) calculated via Prospector using *grzH* photometry (purple) and optical/NIR Nordic Optical Telescope/ALFOSC spectroscopy (green), with the 1σ uncertainty on the spectra shown as a light green envelope. Best-fit photometry is shown as black squares. (Bottom) A zoom in on the black box in the middle plot showing the spectra in more detail, with the H-delta emission line, Calcium H and K absorption lines, and the center of the G band in the rest frame labeled.

following analysis, we used the resulting photometry from this method for the *grz* filters.

We accounted for Galactic extinction by adjusting our photometry using the values reported in Schlafly & Finkbeiner (2011) as implemented by the NASA/IPAC Extragalactic Database (NED) (2019).¹² Finally, zero-point uncertainties and the statistical and systematic uncertainties estimated as above were combined in quadrature to compute total uncertainties for each measurement of each physical object. Table 1 shows total magnitudes for the sum of the three lensed images visible in Figure 1.

4. Stellar Populations in CJ 1323

We derived the properties of stellar populations in CJ 1323 by jointly fitting the spectra and photometry in the image plane with Prospector, an Markov Chain Monte Carlo (MCMC)-based stellar-population synthesis and parameter inference framework (Conroy & Gunn 2010; Foreman-Mackey et al. 2013; Leja et al. 2017; Johnson et al. 2021). We assumed a nonparametric star formation history (SFH). We used seven age bins: 0–50, 50–100, 100–500, 500–1000, 1000–3000,

¹² The NASA/IPAC Extragalactic Database (NED; ned.ipac.caltech.edu/extinction_calculator) is funded by the National Aeronautics and Space Administration and operated by the California Institute of Technology.

Table 1
CJ 1323 Photometry

	<i>g</i>	<i>r</i>	<i>z</i>	<i>H</i>
Total Arc	23.12 ± 0.15	20.66 ± 0.10	18.58 ± 0.10	$17.09^{+0.08}_{-0.09}$

Note. Data is in AB magnitudes, with $\sim 45\%$, 25% , and 30% of the light in images one through three, respectively; *grz*-band imaging is from DECaLS. *H*-band imaging is from Magellan/FOURSTAR infrared imager.

3000–5000, and 5000–5800 Myr in lookback time, with 5800 Myr being the age of the universe at $z = 1.015$. The age bins were represented by the parameters $\log(\text{SFR ratios } n)$, referring to the ratio of total star formation in adjacent time bins. These ratios were fit with a continuity prior (see Leja et al. 2019 for details). We ran our model with 1024 walkers, 1024 iterations, and a burn in = [8192, 4096, 2048, 1024, 512].

We show corner plots constructed via pyGTC (Bocquet & Carter 2016) for two different attenuation curves in Figure 3—the Kriek & Conroy (2013) (K&C13) attenuation curve is blue and the Calzetti et al. (2000) (C+00) attenuation curve is red. We show the results of both models to provide a visual estimate of the systematic uncertainty introduced by how we model the dust attenuation, a variation of which has a more significant impact in our tests than other parameters, e.g., the flexible SFH.

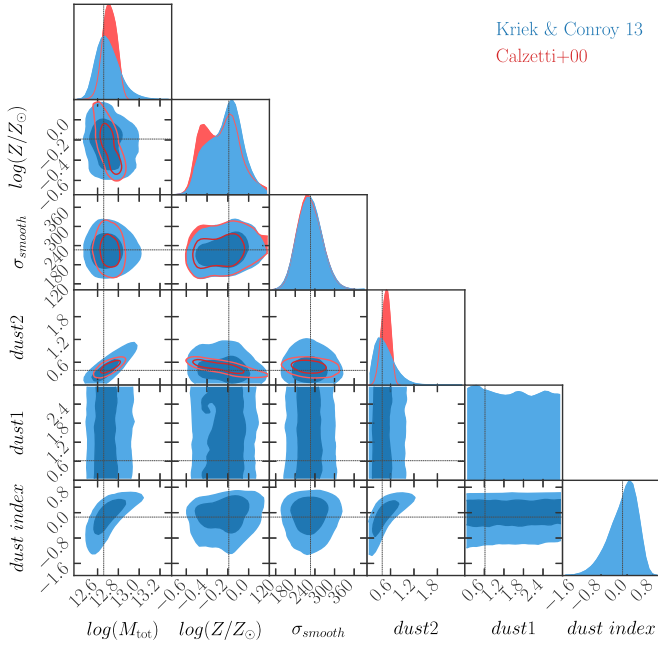


Figure 3. Corner plot with posterior distributions and correlations for inferred parameters in the Prospector SED fitting analysis for the lensed source in the image plane, with contours corresponding to 1σ (dark) and 2σ (light). We show results from the models using the Kriek & Conroy (2013) attenuation curve (blue) and the Calzetti et al. (2000) attenuation curve (red). In the model using the C+00 curve, dust_index is fixed to zero and dust2 is the only normalization factor. The best-fit values for the model using the K&C13 curve are shown with gray dashed lines. This plot clearly shows the results for mass and metallicity are similar regardless of model choice.

Following Leja et al. (2019), we stick to the choice of imposing a continuity prior on the ratio of total star formation in adjacent time bins to allow for smooth transitions of star formation rates (SFRs) between the age bins.

For both models, in addition to the star formation ratios, we simultaneously fit the following free parameters: total mass formed in the galaxy (M_{tot} , in units of solar mass), stellar metallicity $\log(Z/Z_{\odot})$ (where $Z_{\odot} = 0.0142$), velocity smoothing in units of kilometers per second, and spectrum normalization (the ratio of flux between the spectrum and the calibrated photometry) to account for uncertainties in flux and spectral response calibration. For each chain in the MCMC analysis, we calculated the surviving stellar mass (M_*). This accounted for mass loss from stars that have moved off the main sequence, as well as stellar mass locked in stellar remnants, and is used as the mass throughout this Paper.

For the model using the C+00 attenuation curve, dust2 was a free parameter, which sets the overall normalization regardless of the age of stars, in units of opacity at 5500 Å. For the model using the K&C13 attenuation curve, dust1 and dust2 were free parameters, which describe the attenuation of stellar light younger and older than 10^7 yr, respectively. Finally, for the K&C13 model, dust_index (dust slope) was a free parameter, which corresponds to the strength of the 2175 Å UV bump. The stellar mass, metallicity distributions, and SFHs of both models are similar.

We show the best-fit spectral energy distribution (SED) model using the K&C13 dust attenuation curve in Figure 2 and use the results of this model throughout the Paper. The stellar mass and SFH of the arc are found to be robust when fixing stellar metallicity at the best-fit value, $\log(Z/Z_{\odot}) = -0.19$. The

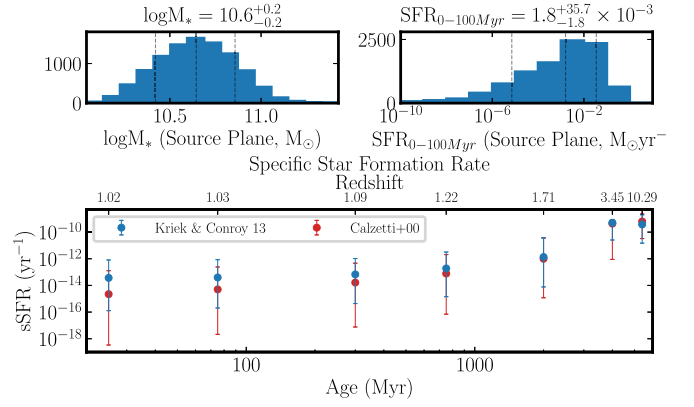


Figure 4. (Top left) The posterior distribution of the demagnified stellar mass of CJ 1323 in the source plane. (Top right) The posterior distribution of the star formation rate (SFR) in the source plane. Both the stellar mass and SFR are the results of the model utilizing the Kriek & Conroy (2013) attenuation curve. The median and uncertainties are reported above each plot and shown as dashed lines. (Bottom) The specific star formation rate for each age bin. Both models show that CJ 1323 was quiescent at the epoch of observation and, within error, show the same rate of star formation.

median value for the stellar mass in the image plane (i.e., the current value) is $\log(M/M_{\odot}) = 12.69^{+0.12}_{-0.09}$. Averaged in the two youngest age bins (0–100 Myr), the best-fit SFR in the image plane is $\text{SFR} = 1.98 M_{\odot} \text{ yr}^{-1}$ with a 1σ upper limit of $2.62 M_{\odot} \text{ yr}^{-1}$ and the specific star formation rate (sSFR) is $\log \text{sSFR} = -12.1 \text{ yr}^{-1}$. We show the sSFR for each age bin in the bottom panel of Figure 4. We find that the best-fit dust index is negative as seen in other quiescent and low-mass galaxies (e.g., Salim et al. 2018; Whitaker et al. 2021; Tacchella et al. 2022), indicating that the attenuation curve is steeper than the Calzetti et al. (2000) curve, where dust_index = 0.

5. Lens Modeling and Source Plane Reconstruction

We modeled the mass distribution using LENSTOOL, a parametric lens modeling tool (Jullo et al. 2007). All halos were treated as pseudoisothermal ellipsoids (dPIEs; Eliásdóttir et al. 2007) with parameters and uncertainties estimated using MCMC sampling. The overall modeling process closely followed the process described in Sharon et al. (2020). Astrometric constraints on the lens model were derived from the GALFIT model of the H -band image (the best seeing image available) without convolving the model with the PSF reference. This was essentially a parametric component deconvolution of the image. Astrometric reference points were placed on matching isophotes, which allowed us to use not just the centroid of each of the visible lensed images but also several locations along each image as constraints on the lens model. The appropriate configuration for these isophote-matched locations was guided by an initial simple model constructed using a single cluster-scale dPIE and smaller halos on each red-sequence cluster galaxy with positions, ellipticity, and position angles tied to the observed stellar light and the other parameters determined via scaling relations. Using the image labeling shown in Figure 1, this initial model strongly suggests two key characteristics for this lensing configuration, namely that: (1) the primary magnification axis of image three is nearly orthogonal to images one and two, and (2) that a fourth image should be present near the bright (and confounding) foreground star in the center of the field. While attempts to recover this fourth image from the initial DECaLS imaging

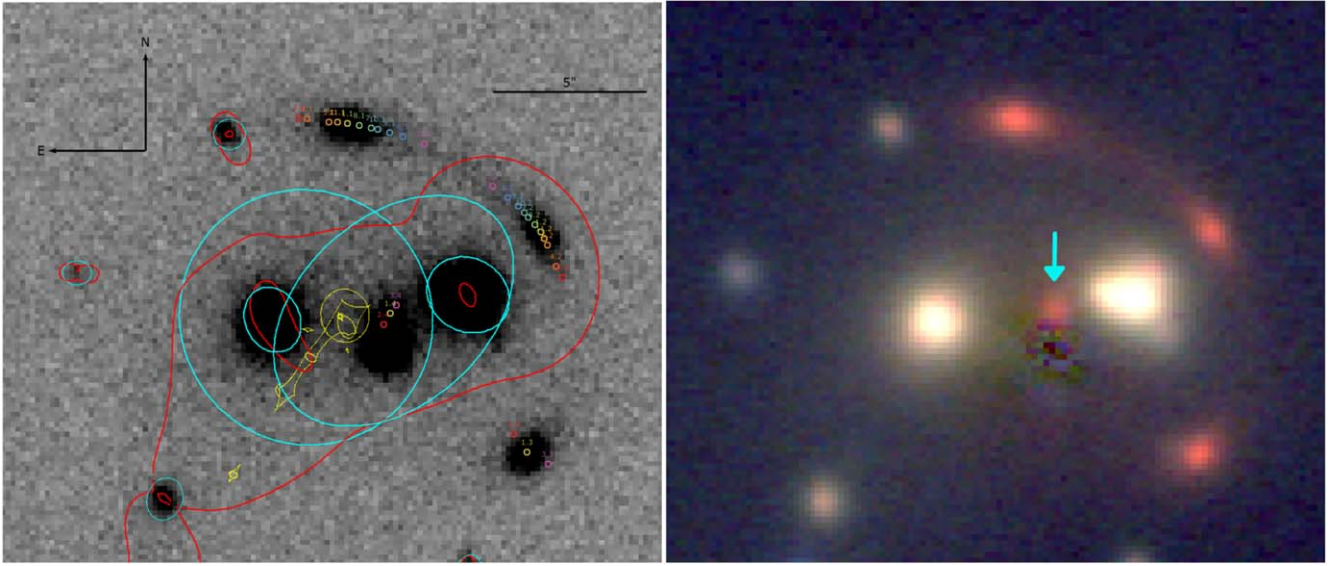


Figure 5. (Left) FOURSTAR *H*-band image of CJ 1323 showing the tangential critical curve from the lens model (red) trisecting the arc and the caustic (yellow). The lens model was made using the positional constraints indicated with small circles. The positional constraints are derived from the *H*-band model, not convolved with the PSF, and each color represents locations of matching surface brightness on the lensed images. (Right) The LDSS3 *grz*-band image, with the central stellar contaminant subtracted, revealing a fourth image. The blue arrow points to the fourth image.

were unsuccessful, additional optical imaging taken as described in Section 3.1 does clearly show the expected fourth image, once the stellar image was fit and removed using GALFIT (see the right panel of Figure 5).

The final lens model used four individually described dPIE components; two fixed on the two visible bright central galaxies, and two cluster-scale halos allowed to vary about those positions. Other cluster-galaxy mass contributions were added via a scaling relation, as described above. The left panel of Figure 5 shows the caustic and critical curves for this final model, and the input constraints derived from the *H*-band image that informs the model. The lens model was optimized in the image plane; the rms position error in the image plane is $0''.26$.

With a final lens model in hand, we reconstructed CJ 1323 in the source plane with PyLenstool, a Python-based wrapper for LENSTOOL.¹³ The reconstructions were made with the unconvolved *H*-band GALFIT model as described above. We added together the source plane reconstructions, centered on the brightest point as determined by a single Sérsic component GALFIT model. We show the combined image in the left panel of Figure 6. We then fit a Sérsic and sky component to the coadded image using GALFIT and report the effective radius, Sérsic index, and axis ratio in Table 2. To understand the variation in the source plane morphology of CJ 1323 introduced by uncertainties in the model, we created combined images using the first ~ 600 realizations of the lens model produced using the bayesCleanlens method in LENSTOOL. We report the median and uncertainty from the GALFIT models of these combined images in Table 2. We find that all source plane reconstructions had $n < 2.5$ and $r_e < 0.8$ kpc, showing that our modeling is robust against degeneracies between n and r_e .

We projected a contour of the image plane half light area into the source plane using the lens model. The resulting area in the source plane divided by the original image plane area is the

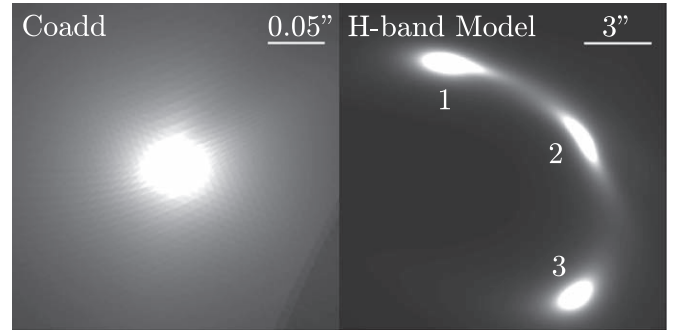


Figure 6. (Left) Coadded reconstructions of COOL J1323+0343 in the source plane. (Right) The GALFIT model of the arc in the image plane based on the FOURSTAR *H*-band data.

Table 2
Source Plane Morphology

Image	R_e	Sérsic Index	Axis Ratio
Best Fit	0.49	2.3	0.88
Posterior Distribution	$0.58^{+0.05}_{-0.08}$	$2.1^{+0.1}_{-0.2}$	$0.87^{+0.02}_{-0.02}$

Note. The top row reports the GALFIT values for the coadd image shown in Figure 6. The second row reports the median with uncertainties from ~ 600 realizations of the lens model, as described in Section 5. The radius is reported in kiloparsecs.

magnification. The best-fit magnifications are $\mu_1 = 55$, $\mu_2 = 31$, and $\mu_3 = 28$ for images one, two, and three, respectively. The best-fit total magnification is $\mu = 113$ and the median is $\mu = 77^{+43}_{-26}$. The magnification uncertainty was found using the same method on ~ 600 realizations of the lens model. This gives a demagnified median $\log M_* = 10.64^{+0.21}_{-0.22} M_\odot$ and the demagnified best-fit SFR = $1.75 \times 10^{-2} M_\odot \text{ yr}^{-1}$ (from 0–100 Myr). The 1σ upper limit on SFR in the image plane is $3.75 \times 10^{-2} M_\odot \text{ yr}^{-1}$. We calculated the errors on the demagnified mass and SFR by sampling the posterior distribution in concert with magnifications from realizations

¹³ <http://pylenstool.readthedocs.io/>

of the lens model. The results are displayed in the top left and right plots in Figure 4.

6. Discussion and Future Work

CJ 1323 is a compact, intermediate-mass quiescent galaxy at $z \sim 1$ —an object difficult to observe without gravitational lensing. We show CJ 1323 and other ETGs at $0.5 < z < 1.5$ in Figure 7 alongside Van der Wel (2014)’s size-mass relation for ETGs at $z = 0.75$ and $z = 1.25$. CJ 1323 is very compact, with only a few other galaxies having comparable effective radii. Its stellar mass is $0.8^{+0.6}_{-0.4}$ times the characteristic mass of the stellar mass function reported in Muzzin et al. (2013) for quiescent galaxies at $1 \leq z < 1.5$. Compared with van der Wel et al. (2014)’s expected size evolution for an ETG with $M_* = 4.4 \times 10^{10}$, CJ 1323 is small at 0.3 times the expected radius at its redshift; 1σ below the relation. Furthermore, the stellar density of CJ 1323 is $\rho = 4^{+8}_{-2} \times 10^{10} M_\odot \text{ kpc}^{-3}$, comparable to compact ETGs at $z = 2.3$ (e.g., Kriek et al. 2008; van Dokkum et al. 2008). This size is consistent with it being an unmodified relic ETG, that is, an early-type galaxy that quenched before $z = 2$ and has not grown since (e.g., Hsu et al. 2014; Stockton et al. 2014; Trujillo et al. 2014; Ferré-Mateu et al. 2017).

The Sérsic index of the combined source plane reconstructions is 2.3, indicating CJ 1323 is more disk-like than a standard $n = 4$ de Vaucouleurs profile. Both observations and simulations find that high-redshift ETGs tend to be disk-like, while those at lower redshifts tend to be more elliptical (van Dokkum et al. 2010; Tacchella et al. 2016). Most samples of intermediate redshift ETGs found that a significant portion of their objects are disk-like (e.g., Stockton et al. 2010; Hsu et al. 2014; Stockton et al. 2014). However, all the source galaxies in Oldham et al. (2017)’s survey of intermediate redshift, $0.4 < z \leq 0.7$, early-type/early-type lens systems had at least one component with $n > 4$. That is, they have a bulge and are not disk-like. As Oldham et al. (2017) noted, this could indicate that their targets are more evolved counterparts of objects like CJ 1323 and the ETGs in previous studies. We caution that source plane reconstructions based on ground-based data are quite uncertain, and the preliminary results on morphology presented here should not be overinterpreted. Nevertheless, the suggestion from the apparent morphology and size is that CJ 1323 is at an early stage of its morphological evolution postquenching.

The SFH makes it clear that CJ 1323 has been quiescent for at least 1 Gyr before the epoch of observation. Man et al. (2021)’s deep spectroscopic study found all three of their lensed quiescent galaxies had short bursts of star formation and then quenched quickly, lying on the $\tau = 0.1$ Gyr quenching curve from Belli et al. (2019). Artificial $U-V$ and $V-J$ colors (1.67 and 0.88, respectively) from the best-fit SED model for CJ 1323 also lie on this curve. Deeper spectroscopy will reveal more about the SFH of CJ 1323, including quenching timescale and age. While better resolution data are needed to fit a more granular SFH, CJ 1323’s SFH, Sérsic index, radius, and stellar density suggest that it has not significantly changed since cosmic noon. If CJ 1323 is an unmodified relic, it will give us the opportunity to study the initial conditions of ETGs in exquisite detail. If not, future studies could uncover evidence for the postquenching evolutionary mechanisms that fuel the growth in radii of ETGs.

The results from this preliminary data make it clear that CJ 1323 is a compelling target. Its total H -band magnitude of 17

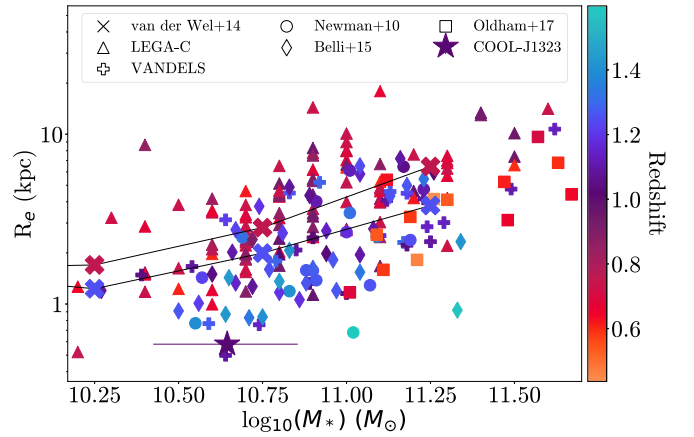


Figure 7. Van der Wel et al. (2014)’s size mass relation for ETGs at $z = 0.75$ and $z = 1.25$ shown with red and purple x’s at the median, respectively, with black lines connecting each point. CJ 1323 is shown with a deep purple star. The color of each object corresponds to its redshift, as defined in the color bar to the right. The other symbols represent ETGs; triangles are quiescent galaxies at $z = 0.6$ –1 reported in Bezanson et al. (2018), drawn from the LEGA-C survey (van der Wel et al. 2016); plus signs are 75 massive quiescent galaxies from $z = 1.0$ –1.3 from the VANDELS survey (Carnall et al. 2019); circles are 17 spheroidals at $z = 1.05$ –1.60 from Newman et al. (2010), diamonds are 40 massive quiescent galaxies at $z = 1.0$ –1.6 from Belli et al. (2014) (the original sample is 56 galaxies; the 16 also in Newman et al. 2010 have been removed), and squares are 13 strongly lensed massive compact ETGs at $z = 0.4$ –0.7 from Oldham et al. (2017). It is clear that, on average, lower redshift galaxies have larger radii, despite there not being as significant a trend for mass. Furthermore, CJ 1323 is one of the most compact galaxies.

makes it one of the two brightest lensed ETGs known, comparable only to MRG-M0138 (Newman et al. 2018; Jafariyazani et al. 2020). CJ 1323 can help probe the processes that cause ETG morphology to change so significantly. Resolved spectra that are in principle possible because of CJ 1323’s extreme magnification would clarify how it quenched by providing a more detailed and better resolved SFH, both spatially and temporally. With sharper imaging, a more constrained lens model could be developed, yielding a more accurate and precise source plane morphology of COOL J1323 +0343, aided by near orthogonal magnifications provided by the different lensed images.

These observations are now being pursued for CJ 1323 and several other lensed ETGs discovered by the COOL-LAMPS collaboration.

We thank the anonymous reviewer for their thoughtful comments. Their efforts have significantly improved this manuscript and the robustness of our results.

This work is supported by The College Undergraduate program at the University of Chicago, and the Department of Astronomy and Astrophysics at the University of Chicago.

G.M. received funding from the European Union’s Horizon 2020 research and innovation programme under the Marie Skłodowska-Curie grant agreement No. 896778.

This Paper includes data gathered with the 6.5 m Magellan Telescopes located at Las Campanas Observatory, Chile.

Based in part on observations made with the Nordic Optical Telescope, operated by the Nordic Optical Telescope Scientific Association at the Observatorio del Roque de los Muchachos, La Palma, Spain, of the Instituto de Astrofísica de Canarias. The data presented here were obtained in part with ALFOSC, which is provided by the Instituto de Astrofísica de Andalucía

(IAA) under a joint agreement with the University of Copenhagen and NOTSA.

Funding for the SDSS and SDSS-II has been provided by the Alfred P. Sloan Foundation, the Participating Institutions, the National Science Foundation, the U.S. Department of Energy, the National Aeronautics and Space Administration, the Japanese Monbukagakusho, the Max Planck Society, and the Higher Education Funding Council for England. The SDSS website is <http://www.sdss.org/>.

The SDSS is managed by the Astrophysical Research Consortium for the Participating Institutions. The Participating Institutions are the American Museum of Natural History, Astrophysical Institute Potsdam, University of Basel, University of Cambridge, Case Western Reserve University, University of Chicago, Drexel University, Fermilab, the Institute for Advanced Study, the Japan Participation Group, Johns Hopkins University, the Joint Institute for Nuclear Astrophysics, the Kavli Institute for Particle Astrophysics and Cosmology, the Korean Scientist Group, the Chinese Academy of Sciences (LAMOST), Los Alamos National Laboratory, the Max-Planck-Institute for Astronomy (MPIA), the Max-Planck-Institute for Astrophysics (MPA), New Mexico State University, Ohio State University, University of Pittsburgh, University of Portsmouth, Princeton University, the United States Naval Observatory, and the University of Washington.

Funding for SDSS-III has been provided by the Alfred P. Sloan Foundation, the Participating Institutions, the National Science Foundation, and the U.S. Department of Energy Office of Science. The SDSS-III website is <http://www.sdss3.org/>.

SDSS-III is managed by the Astrophysical Research Consortium for the Participating Institutions of the SDSS-III Collaboration including the University of Arizona, the Brazilian Participation Group, Brookhaven National Laboratory, Carnegie Mellon University, University of Florida, the French Participation Group, the German Participation Group, Harvard University, the Instituto de Astrofísica de Canarias, the Michigan State/Notre Dame/JINA Participation Group, Johns Hopkins University, Lawrence Berkeley National Laboratory, Max Planck Institute for Astrophysics, Max Planck Institute for Extraterrestrial Physics, New Mexico State University, New York University, Ohio State University, Pennsylvania State University, University of Portsmouth, Princeton University, the Spanish Participation Group, University of Tokyo, University of Utah, Vanderbilt University, University of Virginia, University of Washington, and Yale University.

The Legacy Surveys consist of three individual and complementary projects: the Dark Energy Camera Legacy Survey (DECaLS; NSF's OIR Lab Proposal ID # 2014B-0404; PIs: David Schlegel and Arjun Dey), the Beijing-Arizona Sky Survey (BASS; NSF's OIR Lab Proposal ID # 2015A-0801; PIs: Zhou Xu and Xiaohui Fan), and the Mayall z-band Legacy Survey (MzLS; NSF's OIR Lab Proposal ID # 2016A-0453; PI: Arjun Dey). DECaLS, BASS, and MzLS together include data obtained, respectively, at the Blanco telescope, Cerro Tololo Inter-American Observatory, The NSF's National Optical-Infrared Astronomy Research Laboratory (NSF's OIR Lab); the Bok telescope, Steward Observatory, University of Arizona; and the Mayall telescope, Kitt Peak National Observatory, NSF's OIR Lab. The Legacy Surveys project is honored to be permitted to conduct astronomical research on Iolkam Du'ag (Kitt Peak), a mountain with particular significance to the Tohono O'odham Nation.

The NSF's NOIR Lab is operated by the Association of Universities for Research in Astronomy (AURA) under a cooperative agreement with the National Science Foundation.

This project used data obtained with the Dark Energy Camera (DECam), which was constructed by the Dark Energy Survey (DES) collaboration. Funding for the DES Projects has been provided by the U.S. Department of Energy, the U.S. National Science Foundation, the Ministry of Science and Education of Spain, the Science and Technology Facilities Council of the United Kingdom, the Higher Education Funding Council for England, the National Center for Supercomputing Applications at the University of Illinois at Urbana-Champaign, the Kavli Institute of Cosmological Physics at the University of Chicago, Center for Cosmology and Astro-Particle Physics at the Ohio State University, the Mitchell Institute for Fundamental Physics and Astronomy at Texas A&M University, Financiadora de Estudos e Projetos, Fundação Carlos Chagas Filho de Amparo, Financiadora de Estudos e Projetos, Fundação Carlos Chagas Filho de Amparo a Pesquisa do Estado do Rio de Janeiro, Conselho Nacional de Desenvolvimento Científico e Tecnológico and the Ministerio da Ciência, Tecnologia e Inovação, the Deutsche Forschungsgemeinschaft and the Collaborating Institutions in the Dark Energy Survey. The Collaborating Institutions are Argonne National Laboratory, the University of California at Santa Cruz, the University of Cambridge, Centro de Investigaciones Energéticas, Medioambientales y Tecnológicas-Madrid, the University of Chicago, University College London, the DES-Brazil Consortium, the University of Edinburgh, the Eidgenössische Technische Hochschule (ETH) Zurich, Fermi National Accelerator Laboratory, the University of Illinois at Urbana-Champaign, the Institut de Ciències de l'Espai (IEEC/CSIC), the Institut de Física d'Altes Energies, Lawrence Berkeley National Laboratory, the Ludwig-Maximilians Universität München and the associated Excellence Cluster Universe, the University of Michigan, the National Optical Astronomy Observatory, the University of Nottingham, the Ohio State University, the University of Pennsylvania, the University of Portsmouth, SLAC National Accelerator Laboratory, Stanford University, the University of Sussex, and Texas A&M University.

The Legacy Surveys imaging of the DESI footprint is supported by the Director, Office of Science, Office of High Energy Physics of the U.S. Department of Energy under contract No. DE-AC02-05CH1123, by the National Energy Research Scientific Computing Center, a DOE Office of Science User Facility under the same contract; and by the U.S. National Science Foundation, Division of Astronomical Sciences under contract No. AST-0950945 to NOAO.



This research has made use of the NASA/IPAC Extragalactic Database (NED), which is funded by the National Aeronautics and Space Administration and operated by the California Institute of Technology.

Facilities: Blanco, Magellan:Baade (FOURSTAR), Magellan: Clay (LDSS3), NOT (ALFOSC).

Software: Prospector (Johnson et al. 2021), python-FSPS, SEDpy, pyGTC, Matplotlib (Hunter 2007), Numpy (Harris et al. 2020), Scipy (Virtanen et al. 2020), Astropy (Astropy Collaboration et al. 2013), LENSTOOL, PyLenstool, Jupyter, IPython Notebooks, GALFIT (Peng et al. 2002, 2010), SExtractor (Bertin & Arnouts 1996), SAO Image DS9 (Joye & Mandel 2003), IRAF (Tody 1986, 1993).

ORCID iDs

Ezra Sukay  <https://orcid.org/0000-0002-1106-4881>

Gourav Khullar  <https://orcid.org/0000-0002-3475-7648>
 Michael D. Gladders  <https://orcid.org/0000-0003-1370-5010>
 Keren Sharon  <https://orcid.org/0000-0002-7559-0864>
 Guillaume Mahler  <https://orcid.org/0000-0003-3266-2001>
 Kate Napier  <https://orcid.org/0000-0003-4470-1696>
 Lindsey E. Bleem  <https://orcid.org/0000-0001-7665-5079>
 Håkon Dahle  <https://orcid.org/0000-0003-2200-5606>
 Michael K. Florian  <https://orcid.org/0000-0001-5097-6755>
 Katya Gozman  <https://orcid.org/0000-0003-2294-4187>
 Jason J. Lin  <https://orcid.org/0000-0003-1266-3445>
 Michael N. Martinez  <https://orcid.org/0000-0002-8397-8412>
 Owen S. Matthews Acuña  <https://orcid.org/0000-0001-9225-972X>
 Kaiya Merz  <https://orcid.org/0000-0001-5931-5056>
 Jorge A. Sanchez  <https://orcid.org/0000-0002-9142-6378>
 Emily E. Sisco  <https://orcid.org/0000-0002-2358-928X>
 Daniel J. Kavin Stein  <https://orcid.org/0000-0001-8008-7270>
 Kiyan Tavangar  <https://orcid.org/0000-0001-6584-6144>
 Katherine E. Whitaker  <https://orcid.org/0000-0001-7160-3632>

References

- Akhshik, M., Whitaker, K. E., Brammer, G., et al. 2020, *ApJ*, **900**, 184
 Akhshik, M., Whitaker, K. E., Leja, J., et al. 2021, *ApJL*, **907**, L8
 Astropy Collaboration, Robitaille, T. P., Tollerud, E. J., et al. 2013, *A&A*, **558**, A33
 Belli, S., Newman, A. B., & Ellis, R. S. 2014, *ApJ*, **783**, 117
 Belli, S., Newman, A. B., & Ellis, R. S. 2015, *ApJ*, **799**, 206
 Belli, S., Newman, A. B., & Ellis, R. S. 2019, *ApJ*, **874**, 17
 Bertin, E., & Arnouts, S. 1996, *A&AS*, **117**, 393
 Bezanson, R., van Dokkum, P. G., Tal, T., et al. 2009, *ApJ*, **697**, 1290
 Bezanson, R., van der Wel, A., Pacifici, C., et al. 2018, *ApJ*, **858**, 60
 Bocquet, S., & Carter, F. W. 2016, *JOSS*, **1**, 46
 Calzetti, D., Armus, L., Bohlin, R. C., et al. 2000, *ApJ*, **533**, 682
 Camall, A. C., McLure, R. J., Dunlop, J. S., et al. 2019, *MNRAS*, **490**, 417
 Carollo, C. M., Bschorr, T. J., Renzini, A., et al. 2013, *ApJ*, **773**, 112
 Cassata, P., Giavalisco, M., Guo, Y., et al. 2011, *ApJ*, **743**, 96
 Conroy, C., & Gunn, J. E. 2010, *ApJ*, **712**, 833
 Daddi, E., Renzini, A., Pirzkal, N., et al. 2005, *ApJ*, **626**, 680
 Dawson, K. S., Schlegel, D. J., Ahn, C. P., et al. 2013, *AJ*, **145**, 10
 Dey, A., Schlegel, D. J., Lang, D., et al. 2019, *AJ*, **157**, 168
 Eisenstein, D. J., Weinberg, D. H., Agol, E., et al. 2011, *AJ*, **142**, 72
 Elíasdóttir, Á., Limousin, M., Richard, J., et al. 2007, arXiv:0710.5636
 Fagioli, M., Carollo, C. M., Renzini, A., et al. 2016, *ApJ*, **831**, 173
 Fan, L., Lapi, A., Bressan, A., et al. 2010, *ApJ*, **718**, 1460
 Feldmann, R., Hopkins, P. F., Quataert, E., Faucher-Giguère, C.-A., & Kereš, D. 2016, *MNRAS*, **458**, L14
 Ferré-Mateu, A., Trujillo, I., Martín-Navarro, I., et al. 2017, *MNRAS*, **467**, 1929
 Foreman-Mackey, D., Hogg, D. W., Lang, D., & Goodman, J. 2013, *PASP*, **125**, 306
 Garg, A., Stubbs, C. W., Challis, P., et al. 2007, *AJ*, **133**, 403
 Gladders, M. D., & Yee, H. K. C. 2000, *AJ*, **120**, 2148
 Hao, J., McKay, T. A., Koester, B. P., et al. 2010, *ApJS*, **191**, 254
 Harris, C. R., Millman, K. J., van der Walt, S. J., et al. 2020, *Natur*, **585**, 357
 Hilton, M., Sifón, C., Naess, S., et al. 2021, *ApJS*, **253**, 3
 Hilz, M., Naab, T., & Ostriker, J. P. 2013, *MNRAS*, **429**, 2924
 Hinshaw, G., Larson, D., Komatsu, E., et al. 2013, *ApJS*, **208**, 19
 Hopkins, P. F., Bundy, K., Murray, N., et al. 2009, *MNRAS*, **398**, 898
 Hsu, L.-Y., Stockton, A., & Shih, H.-Y. 2014, *ApJ*, **796**, 92
 Huang, X., Storfer, C., Ravi, V., et al. 2020, *ApJ*, **894**, 78
 Huang, X., Storfer, C., Gu, A., et al. 2021, *ApJ*, **909**, 27
 Hunter, J. D. 2007, *CSE*, **9**, 90
 Jafariyazani, M., Newman, A. B., Mobasher, B., et al. 2020, *ApJL*, **897**, L42
 Johnson, B., Leja, J., Conroy, C., & Speagle, J. 2021, *ApJS*, **254**, 22
 Joye, W. A., & Mandel, E. 2003, in ASP Conf. Ser., 295, Astronomical Data Analysis Software and Systems XII, ed. H. E. Payne, R. I. Jedrzejewski, & R. N. Hook (San Francisco, CA: ASP), 489
 Jullo, E., Kneib, J. P., Limousin, M., et al. 2007, *NJPh*, **5**, 447
 Khullar, G., Gozman, K., Lin, J. J., et al. 2021, *ApJ*, **906**, 107
 Kriek, M., & Conroy, C. 2013, *ApJL*, **775**, L16
 Kriek, M., van Dokkum, P. G., Franx, M., et al. 2008, *ApJ*, **677**, 219
 Lanusse, F., Ma, Q., Li, N., et al. 2018, *MNRAS*, **473**, 3895
 Leja, J., Carnall, A. C., Johnson, B. D., Conroy, C., & Speagle, J. S. 2019, *ApJ*, **876**, 3
 Leja, J., Johnson, B. D., Conroy, C., van Dokkum, P. G., & Byler, N. 2017, *ApJ*, **837**, 170
 Man, A. W. S., Zabl, J., Brammer, G. B., et al. 2021, *ApJ*, **919**, 20
 Miknaitis, G., Pignata, G., Rest, A., et al. 2007, *ApJ*, **666**, 674
 Muzzin, A., Marchesini, D., Stefanon, M., et al. 2013, *ApJ*, **777**, 18
 Naab, T., Johansson, P. H., & Ostriker, J. P. 2009, *ApJL*, **699**, L178
 NASA/IPAC Extragalactic Database (NED) 2019, NASA/IPAC Extragalactic Database (NED), doi:10.26132/ned1
 Newman, A. B., Belli, S., Ellis, R. S., & Patel, S. G. 2018, *ApJ*, **862**, 125
 Newman, A. B., Ellis, R. S., Bundy, K., & Treu, T. 2012, *ApJ*, **746**, 162
 Newman, A. B., Ellis, R. S., Treu, T., & Bundy, K. 2010, *ApJL*, **717**, L103
 Nipoti, C., Treu, T., Leauthaud, A., et al. 2012, *MNRAS*, **422**, 1714
 Oldham, L., Auger, M. W., Fassnacht, C. D., et al. 2017, *MNRAS*, **465**, 3185
 Peng, C. Y., Ho, L. C., Impey, C. D., & Rix, H.-W. 2002, *AJ*, **124**, 266
 Peng, C. Y., Ho, L. C., Impey, C. D., & Rix, H.-W. 2010, *AJ*, **139**, 2097
 Persson, S. E., Barkhouser, R., Birk, C., et al. 2008, *Proc. SPIE*, **7014**, 70142V
 Rest, A., Stubbs, C., Becker, A. C., et al. 2005, *ApJ*, **634**, 1103
 Rykoff, E. S., Rozo, E., Busha, M. T., et al. 2014, *ApJ*, **785**, 104
 Salim, S., Boquien, M., & Lee, J. C. 2018, *ApJ*, **859**, 11
 Schlafly, E. F., & Finkbeiner, D. P. 2011, *ApJ*, **737**, 103
 Sharon, K., Bayliss, M. B., Dahle, H., et al. 2020, *ApJS*, **247**, 12
 Skrutskie, M. F., Cutri, R. M., Stiening, R., et al. 2006, *AJ*, **131**, 1163
 Stockton, A., Shih, H.-Y., & Larson, K. 2010, *ApJL*, **709**, L58
 Stockton, A., Shih, H.-Y., Larson, K., & Mann, A. W. 2014, *ApJ*, **780**, 134
 Strauss, M. A., Weinberg, D. H., Lupton, R. H., et al. 2002, *AJ*, **124**, 1810
 Suess, K. A., Kriek, M., Price, S. H., & Barro, G. 2019a, *ApJ*, **877**, 103
 Suess, K. A., Kriek, M., Price, S. H., & Barro, G. 2019b, *ApJL*, **885**, L22
 Tacchella, S., Dekel, A., Carollo, C. M., et al. 2016, *MNRAS*, **458**, 242
 Tacchella, S., Conroy, C., Faber, S. M., et al. 2022, *ApJ*, **926**, 134
 Tody, D. 1986, *Proc. SPIE*, **627**, 733
 Tody, D. 1993, in ASP Conf. Ser., 52, Astronomical Data Analysis Software and Systems II, ed. R. J. Hanisch, R. J. V. Brissenden, & J. Barnes (San Francisco, CA: ASP), 173
 Trujillo, I., Conselice, C. J., Bundy, K., et al. 2007, *MNRAS*, **382**, 109
 Trujillo, I., Ferré-Mateu, A., Balcells, M., Vazdekis, A., & Sánchez-Blázquez, P. 2014, *ApJL*, **780**, L20
 Trujillo, I., Feulner, G., Goranova, Y., et al. 2006, *MNRAS*, **373**, L36
 van der Wel, A., Franx, M., van Dokkum, P. G., et al. 2014, *ApJ*, **788**, 28
 van der Wel, A., Noeske, K., Bezanson, R., et al. 2016, *ApJS*, **223**, 29
 van Dokkum, P. G., Franx, M., Kriek, M., et al. 2008, *ApJL*, **677**, L5
 van Dokkum, P. G., Whitaker, K. E., Brammer, G., et al. 2010, *ApJ*, **709**, 1018
 Virtanen, P., Gommers, R., Oliphant, T. E., et al. 2020, *NatMe*, **17**, 261
 Wellons, S., Torrey, P., Ma, C.-P., et al. 2015, *MNRAS*, **449**, 361
 Whitaker, K. E., Kriek, M., van Dokkum, P. G., et al. 2012, *ApJ*, **745**, 179
 Whitaker, K. E., Williams, C. C., Mowla, L., et al. 2021, *Natur*, **597**, 485
 Wuyts, E., Barrientos, L. F., Gladders, M. D., et al. 2010, *ApJ*, **724**, 1182
 York, D. G., Adelman, J., Anderson, J. E. J., et al. 2000, *AJ*, **120**, 1579